Soft Matter

RSCPublishing

PAPER

Microparticles confined to a nematic liquid crystal shell

Cite this: *Soft Matter*, 2013, **9**, 6911

Mohamed Amine Gharbi,†[ab] David Seč,[c] Teresa Lopez-Leon,‡[ab] Maurizio Nobili,[ab] Miha Ravnik,[ce] Slobodan Žumer[cde] and Christophe Blanc*[ab]

Received 11th January 2013
Accepted 26th February 2013

DOI: 10.1039/c3sm00126a

www.rsc.org/softmatter

A seminal paper [D. R. Nelson, *Nano Lett.*, 2002, **2**, 1125.] has proposed that a nematic coating could be used to create a valency for spherical colloidal particles through the functionalization of nematic topological defects. Experimental realizations however question the complex behaviour of solid particles and defects embedded in such a nematic spherical shell. In order to address the related topological and geometrical issues, we have studied micrometer-sized silica beads trapped in nematic shells. We underline the mechanisms that strongly modify the texture of the simple (particle-free) shells when colloidal particles are embedded. Finally, we show how the coupling between capillarity and nematic elasticity offers new ways to control the valence and directionality of shells.

1 Introduction

In many aspects, colloidal particles behave as big atoms[1] and their study has thrown a new light on fundamental problems of condensed matter physics, from the kinetics of crystallization to the nature of glassy states. However, common particles lack the ability to interact along specific directions, as atoms do. Introducing anisotropy,[2] inducing a controlled valence[3] and tunable directionality in particle–particle interactions, would extend colloidal science to new problems of condensed matter physics and would enable the fabrication of novel materials with revolutionary technological applications, such as photonic crystals with large band gaps or meta-materials. Important efforts have been made in the last few decades to produce colloidal building blocks displaying directional interactions;[4–6] however, the fabrication of microspheres with a controlled valence is not yet fully available and designing the shape of particles[7,8] is often the main way to reproduce various types of molecular crystals at the micron scale.

A very promising strategy was proposed in a seminal paper by D. Nelson,[9] where he suggested breaking the spherical symmetry of colloidal particles by coating them with a thin nematic liquid crystal (NLC) and taking advantage of the presence of topological defects. Let us recall that a nematic phase is an anisotropic medium usually made of rod-like molecules with an orientational order along a unit vector called the director. In a two-dimensional (2D) nematic phase, the director field might present defects, which are singularities where the director is locally undefined. Some defects are topologically stable[10] and characterized by a topological charge S (called a winding number or an index) that describes the number of 2π-rotations of the director along a path encircling the defect. Experimentally, the charge of a topological defect can be determined by analyzing its optical texture between crossed polarizers.[11,12] The number N of dark brushes (black stripes) around a defect is $N = 4|S|$ and the sign of the charge can be determined by rotating the sample between crossed polarizers. The ground state of a 2D planar nematic phase is characterized by a uniform director field. Topological defects may be generated in out-of-equilibrium textures but these transient structures end up annihilating each other. In contrast, when the nematic phase is confined to more complex geometries, the ground state does not necessarily correspond to a uniform director field and topological defects might persist as stable or metastable objects, either for energetic reasons[13] or for topological ones.[14] For example, when a director field is confined to the strictly 2D surface of a sphere, not only is the spherical symmetry at the surface broken but a set of topological defects of total index $S_t = +2$ is necessarily present.[9,14,15] The strategy proposed by Nelson consists of functionalizing these defects with linkers to induce directional interactions and bonds between the colloidal particles. The number of defects (4 defects of charge $S = +1/2$ or 2 defects of charge $S = +1$ among other possibilities for the sphere) determines the valency of the coating but their position importantly determines the directionality of the binding and could depend continuously on several factors. Additional theoretical works have shown that such a nematic coating could provide control of the valency and the directions, using temperature, shape, elastic constant anisotropy or electric field.[16–21]

---

[a] *Université Montpellier 2, Laboratoire Charles Coulomb UMR5221, F-34095, Montpellier, France. E-mail: Christophe.Blanc02@univ-montp2.fr*

[b] *CNRS, Laboratoire Charles Coulomb UMR5221, F-34095, Montpellier, France*

[c] *Department of Physics, University of Ljubljana, Jadranska 19, 1000 Ljubljana, Slovenia*

[d] *Jožef Stefan Institute, Jamova 39, 1000 Ljubljana, Slovenia*

[e] *Center of Excellence NAMASTE, Jamova 39, 1000 Ljubljana, Slovenia*

† Present address: Department of Physics and Astronomy, University of Pennsylvania, Philadelphia, PA 19104-6396, USA.

‡ Present address: ESPCI-ParisTech, UMR CNRS Gulliver 7083, F-75005 Paris, France.

An experimental model system has been developed in recent years, capable of producing nematic shells as effectively two-dimensional and quasi-two-dimensional spherical nematic fields. A spherical nematic field is spontaneously obtained in water/NLC/water double emulsions,[22,23] provided planar anchoring conditions are present. If the resulting nematic shell is extremely (typically, a few tenths of microns) thin, the ground state is characterized by four defects located at the vertices of a tetrahedron, reproducing the tetrahedral directionality of the sp^3 hybridized orbitals of carbons.[24] The shell thickness inhomogeneity[24,25] and the elastic anisotropy[25,26] have been successfully employed to tune the configurations of defects, opening a way for creating new valences or directionalities.

The issues related to the next step of Nelson's program, *i.e.* the functionalization of these defects, have not been explored yet. From the numerous studies dedicated to NLC–microparticle mixtures, several strategies can be elaborated. For instance, polymers or solid nano-objects can diffuse into the topological defects where the NLC order parameter is lowered[27] or where the elastic energy is confined.[28] Larger particles are also sensitive to the nematic elasticity and spontaneously form aggregates and assemble on disclinations provided that their surfaces are suitably treated. Such effects have been already used in simple geometries, for example, to create microwires along a disclination.[29–32] Similar strategies could therefore be employed with DNA linkers, in order to link coated microspheres together[33–36] and to promote directional bindings. As polymers, the linkers could indeed be trapped by the topological defects, or, alternatively, could be grafted on solid nanoparticles aggregated into the defects. Another approach could consist of trapping a limited and controlled number of larger, already functionalized, particles that will interact with the liquid crystal. In both approaches, mesoscopic particles/aggregates would ultimately interact with the spherical nematic field. This questions the mutual influence of defects and particles confined to a nematic shell. The behaviour of (sub)-micrometer particles in planar nematic layers has been extensively explored in the last few years.[37] The “nematic colloids” are characterized by an intimate relationship with topological defects and by long distance elastic interactions mediated by the nematic matrix. The resulting “structural forces” have been successfully used to create various one-dimensional, two-dimensional and three-dimensional colloidal architectures with microspheres (see for example ref. 38–40, 65) but also, in recent years, with more exotic shapes.[41–43] Other geometries than planar nematic cells however have rarely been studied.

In this paper, we report, for the first time, the behaviour of micrometer sized inclusions trapped to a spherical nematic shell and explore the possibility of using them as possible carriers for transporting ligands toward specific locations on a sphere. After describing the experimental and numerical methods, we demonstrate the local behaviour of a single particle embedded in a spherical nematic field. We discuss the global organization of a shell–particle complex and underline the dominant role of capillarity. Using multiple particles, we show formation of complex patterns and structures and elucidate their trapping. Finally, we discuss the use of large beads for the formation of spherical colloidal particles with controlled valency.

2 Methods

2.1 Experimental

Shells are formed in water/liquid crystal/water double emulsions generated in a microfluidic glass capillary device[22,44] (see Fig. 1a). The coaxial coflow is controlled by three PHD 2000 Harvard Apparatus syringe pumps. The middle fluid is 4′-pentyl-4-cyanobiphenyl (5CB purchased from Synthon). This liquid crystal displays a nematic phase between 17 °C and 35 °C. Both inner and outer fluids are aqueous solutions that contain 1 wt% of polyvinyl alcohol (PVA). The polymer stabilizes the double emulsion and provides a strong planar anchoring at both 5CB/water interfaces. The thickness and size of the shells can be controlled by tuning the liquid flows or by changing their viscosity (*i.e.* adding glycerol in the outer fluid). In some cases, we have also added $CaCl_2$ salt to the inner phase (up to 40 wt%). This yields a slow swelling of the shells due to a tiny water flow through 5CB, due to a difference in osmotic pressure between the inner and outer aqueous phases.[24] The typical nematic shells generated in this way have a final mean radius $\bar{R}$ larger than 30 μm (up to 500 μm) for a mean thickness h_0 in the 0.1–10 μm range.

To trap colloidal inclusions on the shells, we employed silica beads of radius $a = 2 \pm 0.1$ μm purchased from Bangslabs. The solid particles, initially dispersed in an aqueous solution, are first covered by a monolayer of *N*,*N*-dimethyl-*N*-octadecyl-3-aminopropyl trimethoxysilyl chloride (DMOAP purchased from Aldrich) and then dried following ref. 45. This treatment ensures strong homeotropic anchoring of the nematic at the particle surfaces. The beads are then dispersed in 5CB under strong sonication and injected in the capillary device, which ensures that the particles will remain trapped in the liquid crystal (Fig. 1b). After formation, the shells are stabilized in a 1 wt% PVA solution where they can be kept for months with the trapped inclusions still at their surfaces. All subsequent experiments and observations were performed at $T = 23$ °C.

Birefringence patterns are observed with a polarizing microscope (LEICA DM 2500P) equipped with a Sony 1024 × 768 digital camera and a Nikon color camera. The thickness of

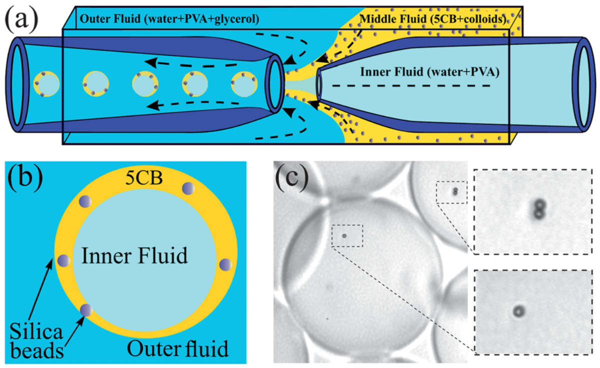

Fig. 1 (a and b) Experimental set-up used to generate the nematic shells. The silica beads are dispersed in the nematic liquid crystal. After the shell formation, they remain confined in the thin nematic layer. We have worked with bead concentrations such that only a single sphere is trapped on a shell ((c) bottom zoomed image). Some shells might display small 2D clusters just after their formation ((c) top zoomed image).

the shells can be determined either directly in bright-field for the thickest shells or from birefringence measurements made with a Berek compensator for the thinnest ones. Note finally that the volume fraction of particles in 5CB remains rather low (typically 0.1%) in order to avoid clogging in the capillary device and to finely control the number of trapped particles at the surface of the shells. At these low bead concentrations, it is possible to generate shells containing a single trapped bead (see Fig. 1c). In the following, we will specifically focus on shells that have a few beads trapped at their surface.

2.2 Modelling

Simulations of nematic textures are performed by using a numerical minimization of the phenomenological Landau-de Gennes free energy based on the tensorial order parameter Q_{ij}:[46]

$$\begin{aligned} F = & \int_{\mathrm{LC}} \left\{ \frac{A}{2} Q_{ij} Q_{ji} + \frac{B}{3} Q_{ij} Q_{jk} Q_{ki} + \frac{C}{4} \left(Q_{ij} Q_{ji} \right)^2 \right\} \mathrm{d}V \\ & + \int_{\mathrm{LC}} \left\{ \frac{L}{2} \frac{\partial Q_{ij}}{\partial x_k} \frac{\partial Q_{ij}}{\partial x_k} \right\} \mathrm{d}V \\ & + \int_{\mathrm{PS}} \left\{ \frac{W_{\mathrm{P}}}{2} \left(\tilde{Q}_{ij} - \tilde{Q}_{ij}^{\perp} \right)^2 \right\} \mathrm{d}S, \\ & + \int_{\mathrm{HS}} \left\{ \frac{W_{\mathrm{H}}}{2} \left(Q_{ij} - Q_{ij}^{0} \right)^2 \right\} \mathrm{d}S, \end{aligned} \tag{1}$$

where LC refers to integration over the bulk of the liquid crystal, PS over the planar degenerate 5CB/water interfaces and HS over the homeotropic surfaces of the beads. The first term accounts for the variation of the nematic degree of order (A, B, and C are material parameters). The second term penalises the elastic distortions from the ordered nematic phase with L being the elastic constant in one-constant approximation. The final two terms model the interaction of the nematic liquid crystal with planar degenerate (anchoring strength W_{P}) and homeotropic surfaces (anchoring strength W_{H}). $\tilde{Q}_{ij}$ and $\tilde{Q}_{ij}^{\perp}$ are related to the full order parameter tensor as defined by Fournier and Galatola,[47] and Q_{ij}^{0} is the surface-preferred order parameter tensor of the homeotropic particle surfaces.

The total free energy is numerically minimized by using an explicit Euler relaxation finite difference scheme on a uniform cubic grid with a grid resolution of 10 nm.[25,46] The surfaces of both shells and inclusions are modeled as closed spherical layers of mesh points, cut out from the grid. The shell surfaces come in close contact at the lower pole; the inclusions are arbitrarily embedded on the upper hemisphere and assumed fixed along the zenithal angle due to capillary effects (see Section 3.3). We typically set the initial conditions for the nematic director in the relaxation algorithm as random spins at each mesh point inside the simulation layer. However, to achieve more targeted design of structures, Ansaetze for the order parameter tensor are also used; for example based on generalized elastic dipoles and quadrupoles.[48] Being only interested in the equilibrium configurations, we neglect the effects of the fluid flow. The following numerical parameters are used: outer shell radius $R_1 = 1$ μm, inner shell radius $R_2 = 0.8$ μm, radius of the bead $a = 0.25$ μm, $L = 8 \times 10^{-12}$ J corresponding to Frank elastic constants $K_1 = K_2 = K_3 = 10.4$ pN, $A = -0.172$ MJ m^{-3}, $B = -2.12$ MJ m^{-3} and $C = 1.73$ MJ m^{-3}; and anchoring strengths $W_{\mathrm{P}} = 10^{-4}$ J m^{-2} and $W_{\mathrm{H}} = 5 \times 10^{-3}$ J m^{-2}. Note that the simulated shells are usually smaller than the experimental ones in order to decrease the computing times. In particular, the ratio between particle size and shell thickness needs to be well matched between experiments and modeling, in order to achieve good agreement. The micrometer size of simulated shells is however closer to the typical size of colloidal particles expected to be suitable for the applications mentioned in the Introduction section.

3 Results and discussion

3.1 Single bead trapped to a shell

We have first examined thin shells (typical thickness of 2–3 μm) decorated with a single bead (Fig. 1c). Between crossed polarizers, the birefringence patterns observed around a particle (see Fig. 2) reveal that the strong homeotropic anchoring on its surface is preserved despite the free PVA present in solution. The polymer ensures the strong planar anchoring at the water/5CB interface but does not interfere with the homeotropic anchoring on the particle.

3.1.1 Topological characterization. When rotating the sample between crossed polarizers, the central area of the bead remains deep black indicating the absence of liquid crystal in this region. If the shell can be considered as very thin (effectively with zero thickness) and having the director strictly in-plane and with zero radial component, the bead can be considered equivalent to a +1 topological defect in a 2D vector field. However, it behaves differently from the common (bulk)

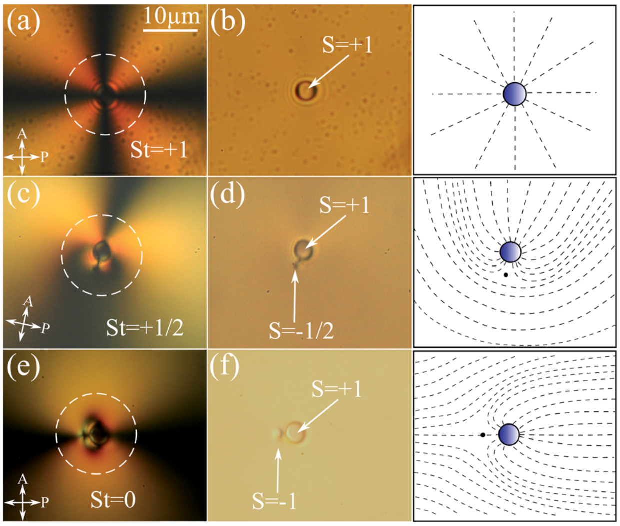

Fig. 2 From top to bottom: a single bead with a homeotropic surface bears a topological charge +1. In a shell, it can be either isolated or closely accompanied by −1/2 or −1 defects, forming a structure with a net charge S_t of value +1, +1/2 or 0 (dipole), respectively. From left to right: micrographs of the particles and the defects between crossed polarizers, in bright field, and a sketch of the 2D director lines around them.

+1 defects observed in thin shells.[24] Here, three different structures are observed in the vicinity of the bead. They are shown and sketched in Fig. 2. The bead is either (i) isolated, or closely accompanied by (ii) a topological defect of charge −1/2 or (iii) a topological defect of charge −1. The microsphere and its neighboring defect are thus topologically equivalent to a single structure with a total topological charge $S_t = +1$, $S_t = +1/2$ or $S_t = 0$ (dipolar structure). Note that the textures we observed recall the ones caused by inclusions with radial anchorings in SmC and SmC* free standing-films.[49,50] However, two main differences are present in smectic membranes. First, detached −1/2 counter-defects are not possible with a polar (c) director. Only surface defects of charge −1/2 can be observed at the surface of the inclusions.[50] Second, a flat membrane favors dipolar and quadrupolar structures of null total charge.

In a thin shell, configurations with different net topological charge are possible, since the spherical confinement just forces the system to have a total (two-dimensional) topological charge of +2, but it does not impose restrictions in the way this charge is achieved. Therefore, in addition to the charge of individual defects, a net charge can remain ascribed to the colloidal inclusion and its neighbouring defect. In 2D, energetically stable defects[11] have a charge of ±1/2 which should enable three different stable configurations. A homeotropic bead would repel +1/2 defects but attract −1/2 defects. Combinations with either one or two −1/2 defects are therefore possible. Any other combination with −1/2 and +1/2 defects would yield an annihilation of defects of opposite signs[51] and give one of the former cases. This simple analysis explains the topological characteristics of observed structures, but cannot account for their energetic stability. For $S_t = 0$ we could expect the bead accompanied by two −1/2 disclinations at the opposite sides of the bead (quadrupolar structure) instead of the observed dipolar structure.

3.1.2 Three-dimensional effects. Finding a dipolar colloidal structure rather than quadrupolar is reminiscent of the competition between dipolar and quadrupolar textures caused by confinement with surfaces or external fields as observed for colloidal beads with homeotropic anchoring in planar nematic cells.[52–55] For a strictly 2D nematic configuration in a plane, the quadrupolar configuration (see Fig. 3a) has a lower elastic free energy[56] than the dipolar one (Fig. 3b). However, here in shells, the energetic competition between dipoles and quadrupoles is determined by two intertwined and mutually coupled effects: (i) the shell geometry and (ii) the actual structure of the defects. As the first effect, in the spherical geometry of the shells with strictly planar surface anchoring, the nematic director is intrinsically curved and distorted, and this curved director field couples differently to the elastic quadrupole than to the elastic dipole. As seen from both experiments and numerical modeling, within the shell, the particles locate in the regions of splay, and indeed only the elastic dipoles have markable splay distortion whereas quadrupoles do not. This enables elastic dipoles to couple more favourably to the general distortion field of the shell by overlapping the splay regions.

As the second effect, the defects of elastic dipoles and quadrupoles in shells are actually not point defects in a 2D vector field but rather short disclination line segments spanning as 3D fields between the two interfaces of the shell (Fig. 3a and b). The defects of an elastic quadrupole are two $S = -1/2$ disclination line segments, whereas the topologically equivalent elastic dipole on the shell has one $S = -1$ disclination line segment. The effective free energy of the disclination lines is known[11] to be proportional to S^2; therefore, from this effect it seems that energetically two −1/2 disclination lines of the quadrupole are more favourable than one −1 disclination of the dipole. However, the integer winding number −1 disclination line segment of the dipole can “escape in the third dimension”,[10] as shown in Fig. 3c and d. Although this well known effect in bulk is expected to be hindered by a strong planar anchoring, it has been shown that a singular line is restored only for thicknesses smaller than a few tens of molecular lengths.[57] In thicker samples (corresponding to our experiments and simulations), the surface anchoring prevents the reorientation only in the vicinity of the plates by forming a pair of surface boojum defects,[57,58] as shown in Fig. 3d. The escape lowers the energetic cost of the disclination core region, and further makes the structure of the elastic dipole – with an escaped −1 disclination – energetically more favourable.

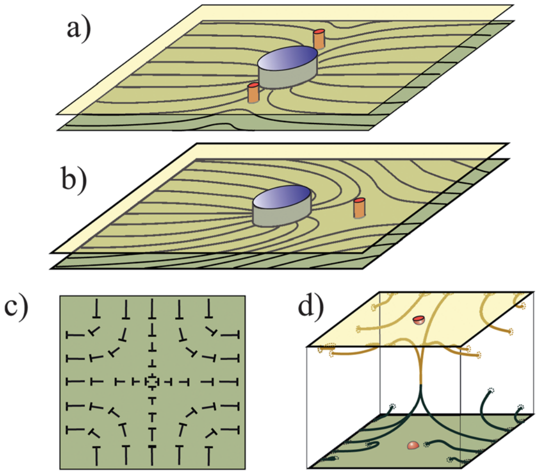

Fig. 3 Circular inclusion with homeotropic surface conditions (*e.g.* a homeotropic sphere with a diameter much larger than the shell thickness) yields a 2D quadrupolar (a) or dipolar (b) configuration when incorporated in a uniform far-field director (integral lines of the director field are shown in the sketches). In a shell, the far-field director of the elastic multipoles becomes distorted. (c and d) Escape in 3D of the −1 disclination line segment. Note the formation of two surface boojum defects at the top and bottom (*i.e.* at the outer and inner interface of the shell).

3.2 Single bead: director field in the shell

Now that the local features of the inclusions have been established, we will focus on the global configurations. Working with a low fraction of particles in 5CB, we have generated a mixture of identical shells with a single bead or without any inclusion at all. The simple particle-free shells display the three combinations of +1/2 and +1 defects shown in Fig. 4. In the 1–10 μm thickness range, a shell is indeed not homogeneous in thickness (see Fig. 4d) and the topological defects are confined to its

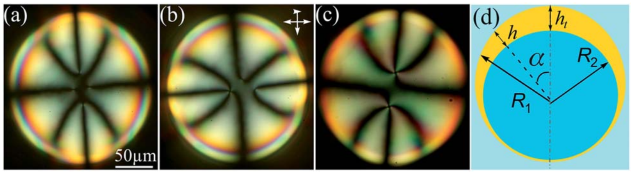

Fig. 4 (a–c) Polarized micrographs of nematic shells without particles (top view). The defects are located in the thinnest region and form one of the three following textures: (a) four +1/2 defects, (b) two +1/2 and one +1 defects, and (c) two +1 defects. (d) Sketch of the side view of a shell. The thickness is non-uniform and is given by $h \approx h_0(1 + \cos\alpha)$ where $h_0 = R_1 - R_2$ is the average thickness. The maximum thickness $h_t = 2h_0$ is observed at the top.

bottom, where the shell is thinner. This heterogeneity in the thickness of a single shell results from the density difference between the salted water and the lighter liquid crystal reinforced by an intrinsic elastic instability of the concentric configuration as we showed in ref. 25. Shells with one bead display distinctive differences. For example, we show in Fig. 5 all the observed configurations that have only free +1/2 defects (they correspond to the two free-particle configurations of Fig. 4a and b). In those thin shells ($h_0 < 3$ μm), the free defects are still located in the thinnest part, but the defect carried by the bead (shown by an arrow) is now located far from the other disclinations, either close to the equator or in the upper hemisphere.

To check that the experimentally observed textures correspond to an equilibrium state and examine in detail the director field, we have simulated the equilibrium (meta)stable states of a shell with a single bead. Indeed, after numerical minimization, we find all three textures observed in experiments. Each texture is presented in Fig. 5 along with the corresponding experimental situation.

The stable configuration (Fig. 5a) consists of two +1/2 disclinations confined to the thinnest part of the shell, while the bead is not accompanied by any defect. The other two configurations are metastable and have more defects. *The second configuration* (Fig. 5b) consists of three +1/2 disclinations at the thinnest part and the microparticle is accompanied by one −1/2 disclination, forming a structure with an effective net charge of $S_t = +1/2$. *In the third state* (Fig. 5c), which has the highest free energy, the solid particle is accompanied by an *escaped* disclination line with winding number −1, forming an elastic dipolar configuration. Topologically, in principle, this −1 disclination could decay into two −1/2 defect lines to form further structures, *e.g.* an elastic quadrupole, however, such transformation is energetically penalised by the energetically unfavourable formation of singular defect cores of the −1/2 disclinations. Therefore, rather than forming two −1/2 disclinations, the −1 disclination escapes in the third dimension, as indicated in Fig. 3. There exists a competition between two different types of anchoring in the vicinity of the microsphere: homeotropic at its spherical surface and planar degenerate at the shell surface, which results in lowering the nematic degree of order in a circular region around the bead (see Fig. 5).

In our numerical treatment, two implicit assumptions are made, which however prove justified upon further consideration, in particular when including capillary effects. First a geometric simplification has been done by considering only simple intersections between spheres and no deformation of

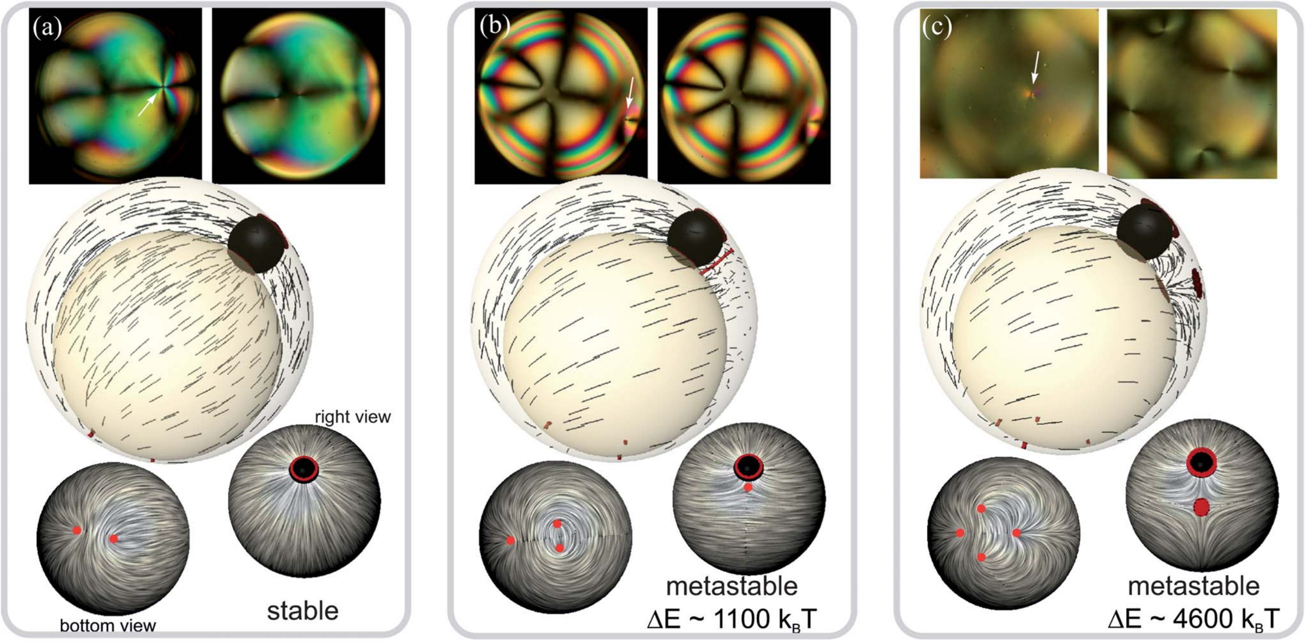

Fig. 5 Polarized micrographs of the three configurations observed for one-bead nematic shells with only free +1/2 disclinations. The particle is usually located on the top shell hemisphere (arrows in the left micrographs) while the free defects reorganize in the thinnest part (right micrographs). The bead and its accompanying disclinations bear an effective net winding number (a) $S_t = +1$, (b) $S_t = +1/2$ and (c) $S_t = 0$. The micrographs are accompanied by the corresponding simulated structures obtained for a shell with one bead located at $\alpha = 45°$ from the z-axis direction. The director field is presented by black lines, and the isosurfaces of the nematic degree of order 0.48 are presented in red.

the shell surfaces. Second, the position of the bead is not a free parameter in the simulations, but is fixed. Which mechanism ultimately controls the vertical position of the bead? A silica bead has a larger density ($\rho_b \approx 2$ g cm^{-3}) than both liquids ($\rho_{5CB} \approx 1.02$ g cm^{-3} for 5CB and $\rho_w \approx 1.3$ g cm^{-3} for salted water). The particle is nevertheless expelled from the bottom region of thin shells which indicates that the weight of the particle is not the driving mechanism, but rather the capillary effects at the surface contact regions.

3.3 The role of capillary effects

At the optical resolution, in bright field, both the inner and outer surfaces of free-particle shells look spherical, which suggests that the capillary effects dominate the nematic elasticity. The 5CB/water surface tension is rather large ($\gamma \approx 26 \times 10^{-3}$ N m^{-1} for pure water[59]), but the presence of polyvinylalcohol slightly decreases this value. Using the rising drop method,[60] we have measured $\gamma \approx 56 \times 10^{-4}$ N m^{-1} for 5CB drops injected in a solution containing 30 wt% of CaCl$_2$ and 1 wt% of PVA. Comparing the maximum gain in elastic energy, of the order of Kh, in a geometry where the surfaces would depart from spheres with a typical additional cost $8\pi\gamma\Delta R^2/5$ (for an ellipsoidal distortion) in interfacial energy, we find that only a very weak relative distortion of the shape, related to the nematic elasticity, is possible for particle-free shells $\Delta R/R \approx \sqrt{5Kh/8\pi\gamma R^2}$, *i.e.* $\Delta R/R \approx 4 \times 10^{-4}$ with typical values $K = 10^{-11}$ N, $R = 50$ μm, $h = 1$ μm and $\gamma = 5$ mN m^{-1}.

For bead–shell complexes, a further analysis has to be done. If the beads are simply confined between inner and outer spherical surfaces, the interface energies are unchanged. Since the inner and outer spheres are not concentric,[25] the local thickness of the shell varies as $h \approx h_0\,(1 + \cos\alpha)$ (see Fig. 4d) when $h_0 \ll R_1$. Therefore, a particle is confined in the thickest regions (lower values of α) and its position should evolve with the average thickness h_0. A change of position during the swelling of shells (*i.e.* while the average thickness h_0 decreases) is indeed experimentally observed. For example, Fig. 6a shows the evolution of two beads confined in a shell during this process. They are first located in the bottom hemisphere and then continuously migrate towards the upper hemisphere when the shell gets thinner. The other possibility to be considered is the trapping of the beads at the water/5CB interfaces. Indeed, a simple stirring is usually sufficient to trap solid particles on the surfaces of the liquid droplets and to form Pickering emulsions.[61] From a geometrical point of view, the trapping of a microsphere on the surface of a liquid spherical droplet is compatible with the Young equation (*i.e.* with a constant contact angle θ_c at the solid/liquid/liquid triple line).[62] Simple geometrical arguments show that trapping at both spherical interfaces of a shell (such as the one sketched in Fig. 4d) is also possible. There is always a position of the bead for which the Young equation is respected at both interfaces, as least as long as its radius a is small enough, typically for $a < h_0/\cos\theta_c$ when $a \ll R_1$. A lower bound should exist, $a > h_m/2\cos\theta_c$, where h_m is the non-vanishing thickness of the nematic film at the south pole, but it is of nanometer order. Since the typical thickness of the films and the diameter of the beads are similar in our experiments, the trapping of the beads at one or at both interfaces has then to be considered. This would be in agreement with the already reported observations that no birefringent effects are observed at the center of the beads.

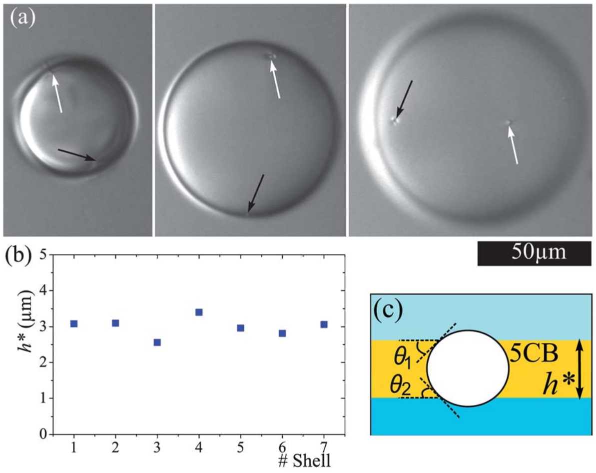

Fig. 6 (a) From left to right: swelling shell observed just after its fabrication, after 2 h and after 12 h. The focus is set on two particles (arrows) confined on the shell. During the swelling, their positions change from the bottom hemisphere to the equator and to the top hemisphere. (b) Local thickness measured around silica beads for various shells and swellings. Its value $h^* = 3.0 \pm 0.3$ μm is nearly constant. (c) At the scale of the bead ($a \ll R_1$), the interfaces are parallel only when the thickness checks $h^* = 2a\cos\theta_c$ where θ_c is the contact angle at the water/5CB/bead triple line. Other thicknesses would yield an extra interfacial energy cost.

An advantage of a nematic film with respect to an isotropic liquid one is that its *local* thickness h can be easily and accurately determined by optical means. In a film nearly perpendicular to the transmitted light, the optical retardation difference δ between the ordinary and extraordinary components is $\delta = h\Delta n$, where Δn is the birefringence ($\Delta n \approx 0.167$ for 5CB[64] at 23 °C). This retardation difference can be accurately determined (with a nm resolution) with a 5λ Berek compensator.[63] The measurement consists of finding the rotation of the compensator's waveplate which "compensates" the birefringence of the sample. The measurement is done locally by minimizing the intensity in a small region (after proper position and orientation of the sample). The lateral accuracy of the region size corresponds to a few pixels of the CCD camera (*i.e.* typically a few microns). We first used the Berek compensator of the polarizing microscope to check optically that the shell thickness was not disturbed by the presence of a microparticle. For example on the top hemisphere, it was found to be almost uniform at a distance of a few diameters from a bead and did not significantly change at large distances in the azimuthal direction. In order to discriminate between the different types of confinement, we have then accurately measured the local thickness h around single beads as follows. A direct measurement can be done when the bead is on the top hemisphere (the optical retardation due to the thin bottom is then negligible). When the bead is closer to the equator or in the bottom hemisphere, the thickness is indirectly obtained. In this case, the optical retardation difference δ is measured at the top of the shell (the compensator is optimally used in this configuration), providing the top shell thickness $h_t = \delta/\Delta n$ and so the average thickness $h_0 = h_t/2$. The projected distance r (± 1 μm) of the focused bead from the shell center gives the 3D zenithal position $\alpha = \arcsin(r/R_1)$ which typically has a resolution of 1° when the bead is far from the equator. When the bead is close to the equator, it is preferable to use the best vertical focus position to determine α with a few degrees of resolution. The local thickness $h \approx h_0(1 + \cos\alpha)$ is then computed from these geometrical parameters, assuming that the shell geometry is unchanged around the bead. Experimental data corresponding to various beads and shells are shown in Fig. 6b. The nearly constant value $h^* \approx 3 \pm 0.3$ μm is smaller than the diameter $2a$ of the beads. This indicates that the silica particles are not simply confined between inner and outer interfaces but are trapped at both 5CB/water interfaces, as sketched in Fig. 6c. Moreover, the deduced contact angle $\theta_c = \arccos(h^*/2a) \approx 40 \pm 10^\circ$ at the silica/water + PVA/5CB triple line is close to the macroscopic one measured for droplets of 5CB deposited on silanized glass and covered by a 1 wt% PVA aqueous solution ($\theta_{c,M} \approx 37 \pm 2^\circ$).

To check the implicit assumption that capillarity dominates elastic effects around the bead, we have considered the effects of a small lateral angular displacement $\Delta\alpha$ of a bead from the geometric position $\alpha^* = \arccos(h^*/h_0 - 1)$. Elastic distortions are locally concentrated around the bead and its defects; the change in elastic free energy is then mainly due to the change in local thickness Δh, *i.e.* $\Delta\mathscr{E}_n = \beta\pi K\Delta h$, where β is a constant of order 1 or 10 (for example, for the 2D texture shown in Fig. 2a, the energy change in a region comprised between the radii $a = 2$ μm and $\mathscr{R} \approx 25$ μm would be $\mathscr{E}_n = K\pi\ln(\mathscr{R}/a)\Delta h \approx 2.5K\pi\Delta h$). The order of change in interfacial energy can be estimated as follows. In the geometry shown in Fig. 6c, the variation in interfacial energy related to the presence of the bead in the 5CB layer is (for both interfaces):

$$\mathscr{E}_b = 4\pi a^2(\gamma_1 - \gamma_2)(1 - \cos\theta) - 2\pi a^2\gamma\sin^2\theta \qquad (2)$$

where γ_1 and γ_2 are the respective interface energy at water/silica and 5CB/silica interfaces. With flat interfaces, this energy is minimal when the contact angle satisfies Young's relationship $\gamma\cos\theta_c = \gamma_1 - \gamma_2$. The Taylor expansion of $\mathscr{E}_b$ around θ_c gives an extra cost $\Delta\mathscr{E}_b \approx 2\pi a^2\gamma\sin^2\theta_c\Delta\theta^2$ for other thicknesses $h = h^* + \Delta h$ and contact angles $\theta = \theta_c + \Delta\theta$. Since $\cos\theta = h/2a$, the extra interfacial energy can be expressed as $\Delta\mathscr{E}_b \approx \pi\gamma\Delta h^2/2$. Comparing $\Delta\mathscr{E}_b$ and $\Delta\mathscr{E}_n$, one obtains an optimal displacement $\Delta h \approx -2\beta K/\gamma$ which corresponds to an angular displacement $\Delta\alpha \approx 2\beta K/\gamma h_0 \sin\alpha^*$. For the following numerical values $K = 10^{-11}$ N, $\gamma = 5.6$ mN m^{-1} and $h_0 \approx 1$ μm, the magnitude $2\beta K/\gamma h_0$ is of order 0.1–1°, which confirms the validity of the geometric approximation for the lateral displacement.

We have checked this analytical model numerically by calculating the free energy of the shells when changing the zenithal position of the bead (the angle α) and also calculating the interfacial energy $\mathscr{E}_b$. For the micrometer-sized shells used in simulations (see Fig. 7a), the variation of the interfacial energy is higher and it would thus primarily affect the positioning of the beads, with the nematic elasticity effectively acting only as a perturbation capable of shifts of a few degrees in α. To achieve direct comparison between modeling and experiments, we have scaled the calculated nematic free energy as $F_s \sim \dfrac{a_{\text{exp}}}{a_{\text{mod}}}F \sim 8F$. Clearly, in these physically larger shells, the nematic free energy proves to be at least an order of magnitude smaller than the interfacial energy (see Fig. 7b). Indeed, as observed in the experiments, the interfacial tension would set the position of the bead, while the nematic elasticity would just slightly perturb its position. Finally, we have also checked that the symmetric positioning of the particle within the shell thickness of Fig. 6c is only weakly disturbed by the liquid crystal elasticity when the spherical geometry (which breaks the up-down symmetry) is taken into account. Fig. 7c shows the nematic free energy variation when the particle is displaced along the radius of the shell. Its minimum remains close to the middle position even for a nonvanishing value of a/R_1.

The bead–shell complexes we have studied can therefore be seen as the result of two uncoupled mechanisms: (i) due to the large interfacial tensions, the spherical shape of the inner and outer interfaces remains almost undisturbed with a varying shell thickness $h \approx h_0(1 + \cos\alpha)$ from its symmetry axis. A bead is confined at a zenithal angular position $\alpha^* = \arccos(h^*/h_0 - 1)$ such that the contact angles $\theta = \theta_c$ are satisfied on both

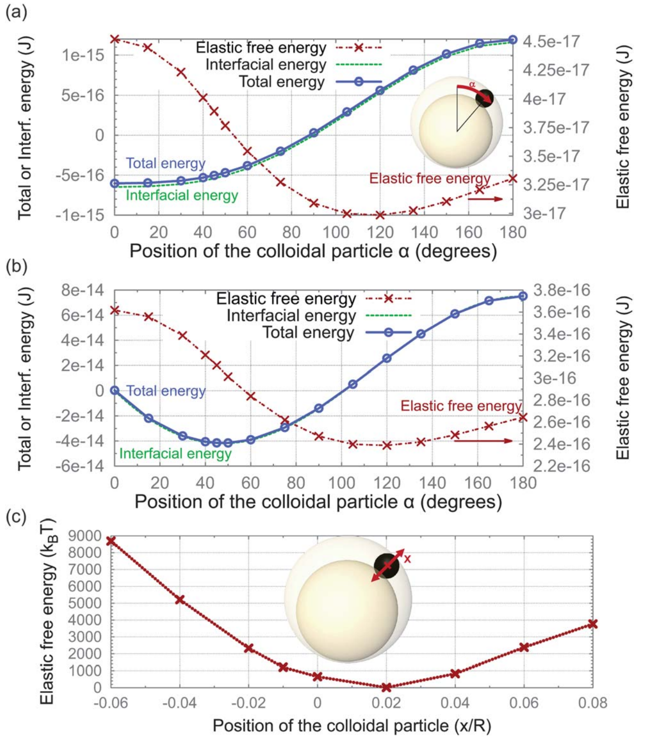

Fig. 7 (a) Nematic elastic free energy (red crosses, right *y* axis) and interfacial energy (green dots, left *y* axis) for shell sizes used in numerical simulations. Note, that the equilibrium position is primarily governed by interfacial energy and for such material parameters the minimum is at $\alpha \sim 0^\circ$. Total energy is the sum of elastic and interfacial energies. (b) Scaled energies for the size of the droplets and beads as in typical experiments ($a \approx 2$ μm). The interfacial energy is much larger than the nematic elasticity and the equilibrium position is at $\alpha \approx 45^\circ$. (c) Total free energy for shifting the bead in the radial direction. The roughly symmetric confinement is preferred by nematic elasticity.

interfaces. (ii) The whole nematic texture then results from the minimization of elastic energy with constraint (i) respected. These rules provide a direct strategy to model and simulate beads trapped to a shell, an otherwise complex problem. Note finally that rule (i) is applicable only for a range of shell thicknesses, *i.e.* $h_0 > h^*/2 \approx 1.5$ μm (for a given bead size $a = 2$ μm). In thinner shells, the bead is confined to the top (thicker part) but the shell shape is necessarily distorted around it [such distortions have already been considered for spherical films of isotropic fluids[62] but, here, the presence of the nematic order yields additional effects that will be discussed in a further work]. The shell axis remains vertical if the relative bead weight (in 5CB) $4/3\pi a^3(\rho_b - \rho_{5CB})$ remains much smaller than the relative weight of the inner sphere $4/3\pi R_1^{\,3}(\rho_w - \rho_{5CB})$, *i.e.* for $a/R_1 \ll \sqrt[3]{(\rho_w - \rho_{5CB})/(\rho_b - \rho_{5CB})}$, which is the case in our experiments. If both liquids have the same density, the non-concentricity is driven only by the elastic forces. The bead then sits exactly at the bottom of the shell and the shell axis is tilted with respect to the vertical. Note finally, that capillarity imposes only the zenithal angle of the bead, not its azimuthal one. This provides an additional control of valency and directionalities of nematic shells that we discuss in the next section.

3.4 Several beads: new valences and patterns

Due to capillarity, beads of identical sizes are all trapped on a circle at the zenithal angle α^*. On this circle, they interact *via* nematic elasticity. When their respective (effectively, two-dimensional) charges S_t are strictly positive, they repel each other and spontaneously create a multivalent shell. For example, when two particles bear the charge $S_t = +1$, they lie on two opposite directions. Fig. 8 shows such a configuration for a shell of average thickness $h_0 \approx h^*$. The beads are then located on the equator at opposite positions along a diameter. Trapping particles in a nematic shell therefore provides a simple way to create a spherical structure with controlled valence. The directionality of the potential bonds imposed by the particles is tunable also by controlling the shell thickness. When the shell gets thinner, the particles shown in Fig. 8a get closer (as already reported in Fig. 6). Although both beads have a positive charge $S_t = +1$, the interaction is dominated by the attractive capillarity effects. Indeed, the interaction energy between two disclinations separated by a distance of d is of order $2\pi K S_t^{\,2} \ln(d/r_c) h$, where r_c is a core radius.[11] Using this scaling and arguments similar to those used in Section 3.3, the typical shift $\Delta\alpha$ from the geometrical position due to elasticity is shown to be smaller than 1° even when the beads are confined at the top of the shell for $h_0 \approx h^*/2$ (see Fig. 8b).

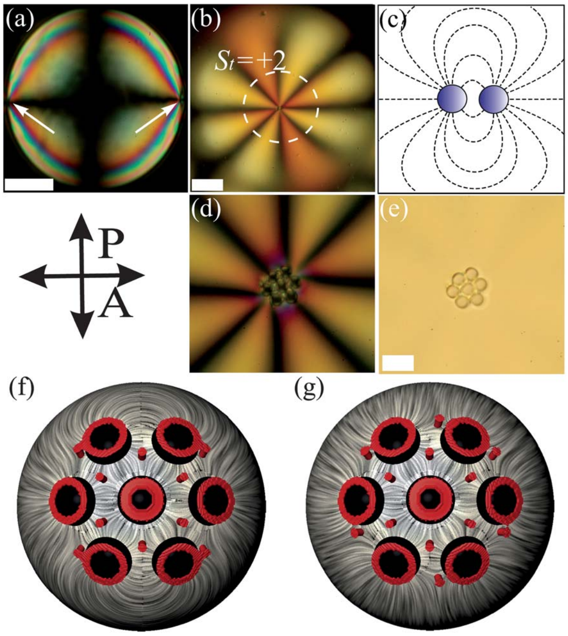

Fig. 8 (a) Shell with two $S_t = +1$ particles observed between crossed polarizers. The mean thickness (≈ 3 μm) forces the beads to lie at the equator and creates a bipolar nematic texture (Bar = 50 μm). (b) Under swelling, the decreasing mean thickness reaches 1.5 μm and the beads are forced to lie at the top forming a single $S_t = +2$ defect sketched in (c). (d and e) Polarized and bright-field micrographs of a more complex colloidal assembly giving a similar global texture. Here, negative topological disclinations are necessarily present within the cluster to balance the +1 topological charges of the beads (Bar = 10 μm). (f and g) Simulated equilibrium structures with 7 beads corresponding to (f) +2 global and (g) +1 global defect textures.

The resulting aggregate has a total charge $S_t = +2$, which results from the charges carried by the two beads, as sketched in Fig. 8c. Due to the presence of particles and their capillary confinement, nematic textures, otherwise unstable in simple shells, can be observed. It should be also noted that different configurations can yield the same nematic textures. For example, Fig. 8d and e display the patterns formed by seven beads confined to the top part of the shell. The texture is similar to the one in Fig. 8b (the total charge of the aggregate is +2) which means that the aggregate is a combination of the beads and associated defects of total charge −5. By simulating configurations with multiple beads many different configurations can be obtained. Two possible (meta)stable states with 7 solid particles are shown in Fig. 8f (with $S_t = +2$) and in Fig. 8g (with $S_t = +1$). Notably, if considering structures of even more particles on the shell, possibly one could go even further and study mechanisms of colloidal crystallisation on a curved (spherical) surface.

4 Conclusions

In this paper, we have investigated the possibility of functionalizing the defects of a nematic shell with micro-sized beads, whose surfaces have been treated to induce normal anchoring in the liquid crystal. Including one of these beads in the nematic phase is topologically equivalent to placing locally one defect of charge +1. In flat geometries, the nematic responds by forming a counter defect so the total charge remains null. In contrast, in nematic shells, we have observed three different defect configurations, where the bead can be: (i) isolated, (ii) accompanied by a defect of charge −1/2 (more precisely, a disclination line segment with winding number −1/2), or (iii) accompanied by a defect of charge −1 (more precisely, a non-singular disclination line segment with winding number −1 and two accompanying surface boojum defects). This richness in configuration is due to the spherical curvature of the confining space, where a total charge of $S_t = +2$ is topologically required.

In the absence of beads, nematic shells typically display isolated defects up to a total charge of $S_t = +2$. The addition of beads modifies the initial defect structure of the experimental shells, which are heterogeneous in thickness. Beads and their associated defects appear at the upper hemisphere of the shell, where it is thicker, due to capillary forces. Since the size of the beads is comparable to the average thickness of the shell, they get trapped simultaneously at the two interfaces delimiting the shell. As a result, the beads and their defects migrate towards a zenithal angle α_c, which depends on the shell thickness, to fulfill the requirements of the Young equation. The rest of the defects organize themselves so that the whole elastic energy is minimal, that is, typically they gather themselves in the lower hemisphere of the shell, where it is thinner.

We have used numerical simulations to demonstrate that the configuration lowest in total (elastic and capillary) free energy is the one displaying an isolated bead at the upper hemisphere and two +1/2 defects at the bottom of the shell. The two other observed configurations are metastable. The number of possible metastable configurations increases drastically when increasing the number of beads in the shell. The beads organize themselves along the circle defined by the critical zenithal angle α_c, in such a way that their mutual distance is maximal, as shown by both experiments and numerical simulations. This configuration can be tuned by varying parameters such as the shell thickness or bead size, offering a way to generate shells with new types of symmetries, valences and directionalities. Simulations furthermore show that similar behaviours are expected for micron-sized shells and submicrometer-sized inclusions. This opens a way for the fabrication of microspheres with complex binding capacities.

Such systems might however be difficult to handle for designing simple and reproducible structures (such as the four-fold symmetry of thin free-particle shells) since capillary effects associated with large beads provoke modifications in the initial symmetry of the shell. It remains to be explored how nano-sized beads behave in nematic shells and if they can be efficiently used to functionalize the disclinations without disturbing them.

Acknowledgements

M.R. acknowledges EU MC Program FREEFLUID. D.S., M.R. and S.Ž. acknowledge ARRS program P1-0099. M.A.G. acknowledges MRSEC DMR11-20901 GRANTS. The authors would like to thank Simon Čopar for reading the manuscript.

References

1 W. Poon, *Science*, 2004, **304**, 830–831.

2 S. C. Glotzer and M. J. Solomon, *Nat. Mater.*, 2007, **6**, 557–562.

3 G. A. DeVries, M. Brunnbauer, Y. Hu, A. M. Jackson, B. Long, B. T. Neltner, O. Uzun, B. H. Wunsch and F. Stellacci, *Science*, 2007, **315**, 358–361.

4 E. C. Nelson and P. V. Braun, *Science*, 2007, **318**, 924–925.

5 Q. Chen, J. K. Whitmer, S. Jiang, S. C. Bae, E. Luijten and S. Granick, *Science*, 2011, **331**, 199–202.

6 Q. Chen, S. C. Bae and S. Granick, *Nature*, 2011, **469**, 381–384.

7 L. Rossi, S. Sacanna, W. T. M. Irvine, P. M. Chaikin, D. J. Pine and A. P. Philipse, *Soft Matter*, 2011, **7**, 4139–4142.

8 J. D. Forster, J. G. Park, M. Mittal, H. Noh, C. F. Schreck, C. S. O'Hern, H. Cao, E. M. Furst and E. R. Dufresne, *ACS Nano*, 2011, **5**, 6695–6700.

9 D. R. Nelson, *Nano Lett.*, 2002, **2**, 1125.

10 M. Kleman and O. D. Lavrentovich, *Soft Matter Physics: An Introduction*, Springer-Verlag, New York, 2003.

11 P. G. de Gennes and J. Prost, *The Physics of Liquid Crystals*, Oxford Science Publications, Oxford, 2nd edn, 1993.

12 P. Oswald and P. Pieranski, *Nematic and Cholesteric Liquid Crystals: Concepts and Physical Properties Illustrated by Experiments*, Taylor & Francis, CRC, Boca Raton, FL, 2005.

13 B. L. Mbanga, G. M. Grason and C. D. Santangelo, *Phys. Rev. Lett.*, 2012, **108**, 017801.

14 T. C. Lubensky and J. Prost, *J. Phys. II*, 1992, **2**, 371.

15 H. Poincaré, *J. Math. Pure. Appl.*, 1885, **1**, 167.

16 M. A. Bates, *J. Chem. Phys.*, 2008, **128**, 104707.

17 M. A. Bates, G. Skačej and C. Zannoni, *Soft Matter*, 2010, **6**, 655.

18 S. Dhakal, F. J. Solis and M. Olvera de la Cruz, *Phys. Rev. E: Stat., Nonlinear, Soft Matter Phys.*, 2012, **86**, 011709.

19 G. Skacej and C. Zannoni, *Phys. Rev. Lett.*, 2008, **100**, 197802.

20 S. Kralj, R. Rosso and E. Virga, *Soft Matter*, 2011, **7**, 670.

21 H. Shin, M. J. Bowick and X. J. Xing, *Phys. Rev. Lett.*, 2008, **101**, 037802.

22 A. Fernandez-Nieves, V. Vitelli, A. S. Utada, D. R. Link, M. Marquez, D. R. Nelson and D. A. Weitz, *Phys. Rev. Lett.*, 2007, **99**, 157801.

23 T. Lopez-Leon and A. Fernandes-Nieves, *Colloid Polym. Sci.*, 2011, **289**, 345.

24 T. Lopez-Leon, V. Koning, K. B. S. Devaiah, V. Vitelli and A. Fernandez-Nieves, *Nat. Phys.*, 2011, **7**, 391.

25 D. Seč, T. Lopez-Leon, M. Nobili, Ch. Blanc, A. Fernandez-Nieves, M. Ravnik and S. Žumer, *Phys. Rev. E: Stat., Nonlinear, Soft Matter Phys.*, 2012, **86**, 020705(R).

26 T. Lopez-Leon, A. Fernandes-Nieves, M. Nobili and C. Blanc, *Phys. Rev. Lett.*, 2011, **106**, 247802.

27 S. Samitsu, Y. Takanishi and J. Yamamoto, *Nat. Mater.*, 2010, **9**, 816.

28 O. D. Lavrentovich, *Proc. Natl. Acad. Sci. U. S. A.*, 2011, **108**, 5143.

29 M. Škarabot, M. Ravnik, S. Žumer, U. Tkalec, I. Poberaj, D. Babič and I. Muševič, *Phys. Rev. E: Stat., Nonlinear, Soft Matter Phys.*, 2008, **77**, 061706.

30 M. Ravnik, G. P. Alexander, J. M. Yeomans and S. Žumer, *Faraday Discuss.*, 2010, **144**, 159.

31 H. Agha, J.-B. Fleury and Y. Galerne, *Eur. Phys. J. E*, 2012, **35**, 82.

32 J.-B. Fleury, D. Pires and Y. Galerne, *Phys. Rev. Lett.*, 2009, **103**, 267801.

33 S. Y. Park, A. K. R. Lytton-Jean, B. Lee, S. Weigand, G. C. Schatz and C. A. Mirkin, *Nature*, 2008, **451**, 553–556.
34 D. Nykypanchuk, M. M. Maye, D. van der Lelie and O. Gang, *Nature*, 2008, **451**, 549–552.
35 R. J. Macfarlane, *et al.*, *Science*, 2011, **334**, 204–208.
36 P. L. Biancaniello, A. J. Kim and J. C. Crocker, *Phys. Rev. Lett.*, 2005, **94**, 4.
37 See a recent topical review in I. Muševič, M. Škarabot and M. Humar, *J. Phys.: Condens. Matter*, 2011, **23**, 284112.
38 I. Muševič, M. Škarabot, U. Tkalec, M. Ravnik and S. Žumer, *Science*, 2006, **313**, 954.
39 U. Ognysta, A. Nych, V. Nazarenko, I. Muševič, M. Škarabot, M. Ravnik, S. Žumer, I. Poberaj and D. Babič, *Phys. Rev. Lett.*, 2008, **100**, 217803.
40 U. Ognysta, A. Nych, V. Nazarenko, M. Škarabot and I. Muševič, *Langmuir*, 2009, **25**, 12092.
41 B. Senyuk, Q. Liu, S. He, R. D. Kamien, R. B. Kusner, T. C. Lubensky and I. I. Smalyukh, *Nature*, 2013, **493**, 200–205.
42 B. Senyuk and I. I. Smalyukh, *Soft Matter*, 2012, **8**, 8729.
43 C. P. Lapointe, T. G. Mason and I. I. Smalyukh, *Science*, 2009, **326**, 1083–1086.
44 A. S. Utada, E. Lorenceau, D. R. Link, P. D. Kaplan, H. A. Stone and D. A. Weitz, *Science*, 2005, **308**, 537.
45 M. A. Gharbi, M. Nobili, M. In, G. Prévot, P. Galatola, J.-B. Fournier and Ch. Blanc, *Soft Matter*, 2011, **7**, 1467–1471.
46 M. Ravnik and S. Žumer, *Liq. Cryst.*, 2009, **36**, 1201.
47 J. B. Fournier and P. Galatola, *Europhys. Lett.*, 2005, **72**, 403.
48 T. C. Lubensky, D. Pettey, N. Currier and H. Stark, *Phys. Rev. E: Stat. Phys., Plasmas, Fluids, Relat. Interdiscip. Top.*, 1998, **57**, 610.
49 P. Cluzeau, P. Poulin, G. Joly and H. T. Nguyen, *Phys. Rev. E: Stat., Nonlinear, Soft Matter Phys.*, 2001, **63**, 031702.
50 P. V. Dolganov, H. T. Nguyen, E. I. Kats, V. K. Dolganov and P. Cluzeau, *Phys. Rev. E: Stat., Nonlinear, Soft Matter Phys.*, 2007, **75**, 031706.
51 C. Blanc, D. Svensek, S. Žumer and M. Nobili, *Phys. Rev. Lett.*, 2005, **95**, 097802.
52 Y. Gu and N. L. Abbott, *Phys. Rev. Lett.*, 2000, **85**, 4719–4722.
53 H. Stark, *Phys. Rev. E: Stat., Nonlinear, Soft Matter Phys.*, 2002, **66**, 032701.
54 C. Völtz, Y. Maeda, Y. Tabe and H. Yokoyama, *Phys. Rev. Lett.*, 2006, **97**, 227801.
55 M. Škarabot, M. Ravnik, S. Žumer, U. Tkalec, D. Babič, N. Osterman and I. Muševič, *Phys. Rev. E: Stat., Nonlinear, Soft Matter Phys.*, 2008, **77**, 031705.
56 J. Fukuda and H. Yokoyama, *Eur. Phys. J. E*, 2001, **4**, 389–396.
57 C. Chiccoli, I. Feruli, O. D. Lavrentovich, P. Pasini, S. V. Shiyanovskii and C. Zannoni, *Phys. Rev. E: Stat., Nonlinear, Soft Matter Phys.*, 2002, **66**, 030701(R).
58 V. Vitelli and D. R. Nelson, *Phys. Rev. E: Stat., Nonlinear, Soft Matter Phys.*, 2006, **74**, 021711.
59 J. E. Proust, E. Perez and L. Ter-Minassian-Saraga, *Colloid Polym. Sci.*, 1978, **256**, 666–681.
60 J. W. Kim, H. Kim, M. Lee and J. J. Magda, *Langmuir*, 2004, **20**, 8110–8113.
61 B. P. Binks, *Curr. Opin. Colloid Interface Sci.*, 2002, **7**, 21.
62 P. A. Kralchevsky and K. Nagayama, *Adv. Colloid Interface Sci.*, 2000, **85**, 145.
63 D. B. Murphy, *Fundamentals of Light Microscopy and Electronic Imaging*, Wiley, New York, 2001.
64 K. C. Chu, C. K. Chen and Y. R. Shen, *Mol. Cryst. Liq. Cryst.*, 1980, **59**, 97.
65 A. Nych, U. Ognysta, M. Škarabot, M. Ravnik, S. Žumer and I. Muševič, *Nat. Commun.*, 2013, **4**, 1489.